
VICON: A Foundation Model for Multi-Physics Fluid Dynamics via Vision In-Context Operator Networks

Yadi Cao^{*1,2} Yuxuan Liu^{*2} Liu Yang^{3,2} Rose Yu¹ Hayden Schaeffer² Stanley Osher²

Abstract

In-Context Operator Networks (ICONS) are models that learn operators across different types of PDEs using a few-shot, in-context approach. Although they show successful generalization to various PDEs, existing methods treat each data point as a single token, and suffer from computational inefficiency when processing dense data, limiting their application in higher spatial dimensions. In this work, we propose *Vision In-Context Operator Networks* (VICON), incorporating a vision transformer architecture that efficiently processes 2D functions through patch-wise operations. We evaluated our method on three fluid dynamics datasets, demonstrating both superior performance (reducing the rescaled L^2 error by 40% and 61.6% for two benchmark datasets for compressible flows, respectively) and computational efficiency (requiring only one-third of the inference time per frame) in long-term rollout predictions compared to the current state-of-the-art sequence-to-sequence model with fixed timestep prediction: Multiple Physics Pretraining (MPP). Compared to MPP, our method preserves the benefits of in-context operator learning, enabling flexible context formation when dealing with insufficient frame counts or varying timestep values.

1. Introduction

Machine learning has recently emerged as a powerful tool for solving Partial Differential Equations (PDEs). Traditional approaches primarily operate on discrete representations, with Convolutional Neural Networks (CNNs) excelling at processing regular grids (Gupta & Brandstetter, 2022) and Graph Neural Networks (GNNs) handling un-

structured meshes (Sanchez-Gonzalez et al., 2020; Lino et al., 2022; Cao et al., 2023). Although recent developments have incorporated transformer architectures to capture global dependencies (Cao, 2021), these discrete approaches often face two key limitations: they lack explicit PDE context information and are confined to operating on fixed or similar topologies.

Several methods have emerged to address these limitations. The Deep Galerkin Method (DGM) (Sirignano & Spiliopoulos, 2018), Deep Ritz Method (DRM) (E & Yu, 2018), and Physics-Informed Neural Networks (PINN) (Raissi et al., 2019) incorporate PDE constraints in the model loss terms. The model, once trained, becomes a surrogate solution that can be queried at any location in the domain. However, these methods typically require complete retraining when initial or boundary conditions change. This limitation led to the development of “operator learning,” where neural networks map input functions to output functions, such as from initial conditions to later-time solutions. This capability was first demonstrated using shallow neural networks (Chen & Chen, 1995b;a), followed by specialized architectures such as the widely-adopted Fourier Neural Operator (FNO) (Li et al., 2021; Kovachki et al., 2023), Deep Operator Network (DeepONet) (Lu et al., 2021), and recent attempts to incorporate transformers as operator learners (Li et al., 2022).

Although the aforementioned methods excel at learning individual, single operators, they are not able to generalize across different operators. This limitation necessitates costly retraining for new equation parameters or predicting with longer time horizons. Inspired by the success of large language models (LLMs) in multi-domain generation, recent work has explored “PDE foundation models”. Common approaches employ pre-training and fine-tuning strategies (Chen et al., 2024; Herde et al., 2024; Zhang et al., 2024c), though these require additional deployment resources. To achieve zero-shot PDE foundation models, additional information is often needed, for example, the PROSE approach (Liu et al., 2024b;a; Sun et al., 2024a; Jollie et al., 2024) encodes the governing equations directly through symbolic information. Other approaches achieve zero- or few-shot generalization by using directed graphs to

^{*}Equal contribution ¹University of California, San Diego ²University of California, Los Angeles; Work partially done when Yadi Cao and Liu Yang were at UCLA. ³National University of Singapore. Correspondence to: Stanley Osher <sjos@math.ucla.edu>.

represent equations (Ye et al., 2024) or symbol tokenization (Lorsung et al., 2024).

While these approaches require explicit encoding of PDE information, which may not be readily available or precisely known in practice, the In-Context Operator Network (ICON) (Yang et al., 2023a) offers a fundamentally different approach. ICON implicitly encodes system dynamics through input-output function pairs (before-after operators), achieving a few-shot generalization without retraining or explicit PDE knowledge. A single ICON model has shown success in handling both forward and inverse problems in various ODEs, PDEs, and mean field control scenarios.

However, ICON’s computational efficiency becomes a critical bottleneck when handling dense data in higher dimensions. Specifically, representing each spatial point as an individual token leads to quadratic complexity in the number of points, making it computationally prohibitive for practical 2D and 3D applications - to date, only one instance of a 2D case (Yang et al., 2023a) using sparse data points has been demonstrated.

To address this limitation, we propose *Vision In-Context Operator Networks* (VICON), which leverage vision transformers to process 2D functions using an efficient patch-wise approach. Going beyond classic vision transformers, which typically process patches from a single image, VICON extends the architecture to handle sequences of input-output function pairs, allowing “next function prediction” capabilities while preserving the benefits of in-context operator learning. Our contributions include:

- Development of VICON, a vision transformer-based in-context operator network for two-dimensional time-dependent PDEs that maintains the in-context operator learning framework and handles dense data points in higher dimensions.
- We evaluated our model across diverse fluid dynamics systems, comprising 879K frames with varying timestep sizes. Empirical results demonstrate significant improvements over the state-of-the-art MPP (McCabe et al., 2023), including a 40% and 61.6% reduction in the scaled L2 error for long-term predictions in two benchmark datasets, a 67% reduction in the prediction error of turbulence kinetic energy, and approximately one third of the single step inference time.
- VICON enables flexible rollout scheme unattainable by traditional sequence-to-sequence models: it can form example pairs from nonsequential time sequences, handle scenarios with insufficient example frames, and adapt to varying timestep strides without retraining. These capabilities allow for robust rollout even with incomplete or irregularly sampled temporal data.

2. Related Works

Operator Learning Operator learning (Chen & Chen, 1995b;a; Li et al., 2021; Lu et al., 2021) addresses the challenge of approximating operators $G : U \rightarrow V$, where U, V are function spaces. These operators usually model solutions of physical systems and differential equations, representing the map from initial/boundary conditions and parameters to equation solutions. DeepONets (Lu et al., 2021; 2022) use branch and trunk networks to separately process inputs and query points, and have been extended to handle multiple input parametric functions in MIONet (Jin et al., 2022). FNOs (Li et al., 2021) leverage kernel integration approximations for PDE solutions by processing features in Fourier space, where kernel integrations can be efficiently computed through multiplications. These methods have been further extended to incorporate equation information (Wang et al., 2021), multiscale features (Zhang et al., 2024a; Wen et al., 2022), different input/output meshes (Zhang et al., 2023), complex geometries (Li et al., 2024), and distributed learning (Zhang et al., 2024b). The applications of operator learning include weather prediction (Pathak et al., 2022; Jiang et al., 2024), biology (Yin et al., 2024), and uncertainty quantification (Moya et al., 2024). However, these approaches are typically designed to learn a single operator, requiring retraining when encountering different types of PDE or time-step sizes.

PDE Foundation Models Foundation models are large-scale, pre-trained models that serve as versatile building blocks for a wide range of downstream tasks in natural language processing (Brown et al., 2020; Touvron et al., 2023), computer vision (Ramesh et al., 2021), and other AI applications. However, they are not directly applicable to scientific computing tasks such as the discovery of PDEs (Schaeffer, 2017) or computational fluid dynamics (Wang et al., 2024), where high precision is essential. Recent work has explored adapting the principles of the foundation model to PDEs through various approaches. Some methods employ pre-training and fine-tuning strategies (Chen et al., 2024; Herde et al., 2024), though this requires additional computational resources during deployment. Zero-shot PDE foundation models incorporate additional information; for example, the PROSE approach (Liu et al., 2024b;a; Sun et al., 2024a; Jollie et al., 2024) encodes the PDE directly through symbolic information, which can also be fine-tuned (Sun et al., 2024b). Other models achieve zero- or few-shot generalization by adding PDE structures to the network (Lorsung et al., 2024; Ye et al., 2024); however, these methods require prior knowledge of the PDE structure and information on the data.

In-Context Operator Networks ICONs (Yang et al., 2023a;b; Yang & Osher, 2024) learn operators through

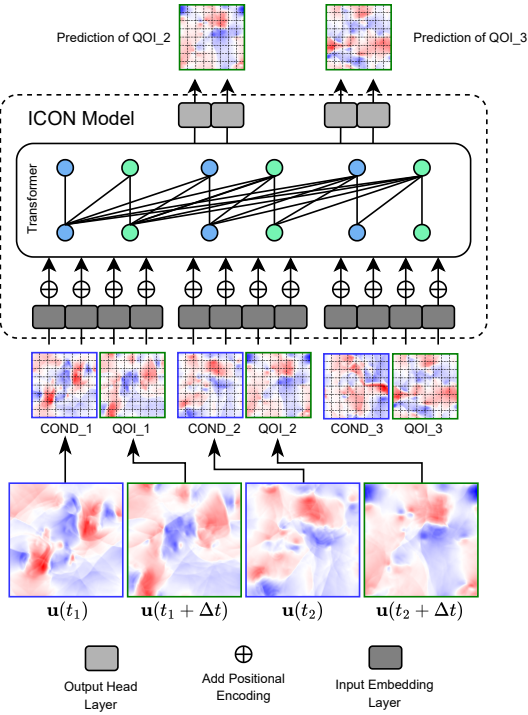


Figure 1. VICON model overview. The inputs to the model are pairs of conditions (COND) and quantities of interest (QOI), which are patchified and flattened before feeding into the transformer layers. The outputs, which represent different patches in the output frame, are transformed back to obtain the final predictions.

observing input-output function pairs, enabling few-shot generalization across various PDEs without explicit PDE representation or fine-tuning. ICONs have demonstrated success in handling forward and inverse problems in ODEs, PDEs, and mean-field control scenarios. However, they face significant computational challenges when processing dense data, as they represent functions through scattered point tokens, resulting in quadratic computational complexity. This limitation has largely restricted their application to 1D problems, with only sparse sampling possible in 2D cases. Our work addresses these limitations by introducing a vision transformer architecture that efficiently handles dense 2D data while maintaining the benefits of in-context operator learning.

3. Preliminaries

ICONs were introduced and developed in (Yang et al., 2023a;b; Yang & Osher, 2024). They adapt the in-context learning framework from large language models, aiming to train a model that can learn operators from prompted

function examples.

Denote an ICON model as \mathcal{T}_θ , where \mathcal{T} is a transformer with trainable parameters θ . The model takes input as a sequence comprising I pairs of conditions (c) and quantities of interest (q) as $\{\langle c_i, q_i \rangle\}_{i=1}^I$, where each c, q contains multiple tokens representing a single function. The model outputs tokens representing future functions at the positions of c , i.e. “next function prediction” similar to “next token predictions” in LLM. More precisely, for $J \in \{1, \dots, I - 1\}$, the model predicts \tilde{q}_{J+1} given the leading J pairs and the condition c_{J+1} :

$$\tilde{q}_{J+1} = \mathcal{T}_\theta[c_{J+1}; \{\langle c_i, q_i \rangle\}_{i=1}^J]. \quad (1)$$

For training parallelization, ICON uses a special causal attention mask to perform autoregressive learning (i.e., the model only sees the leading J pairs and c_{J+1} when predicting \tilde{q}_{J+1}) and enables output of all predictions within a single forward pass (Yang et al., 2023b):

$$\{\tilde{q}_i\}_{i=1}^I = \mathcal{T}_\theta[\{\langle c_i, q_i \rangle\}_{i=1}^I]. \quad (2)$$

Training loss is computed as the mean squared error (MSE) between the predicted states \tilde{q}_i and the ground truth states q_i . To ensure that the model receives sufficient contextual information about the underlying dynamics, we only compute errors for the indices $i > I_{\min}$, effectively requiring at least I_{\min} examples in context. This approach has demonstrated empirical improvements in model performance.

After training, ICON can process a new set of $\langle c, q \rangle$ pairs in the forward pass to in-contextually learn operators and employ them to predict future functions using new conditions:

$$\tilde{q}_k = \mathcal{T}_\theta[c_k; \{\langle c_i, q_i \rangle\}_{i=1}^J], \quad (3)$$

where $J \in \{I_{\min}, \dots, I - 1\}$ is the number of in-context examples, and $k > I$ is the index of the condition for future prediction.

Importantly, all pairs in the same sequence must be formed with the same operator mapping (i.e., the same PDE and consistent timestep size), while operators can vary across different sequences.

4. Methodology

4.1. Problem Setup

We consider the forward problem for multiple time-dependent PDEs that are *temporally homogeneous Markovian*, defined on domain $\Omega \subseteq \mathbb{R}^2$ with solutions represented by $\mathbf{u}(\mathbf{x}, t) : \Omega \times [0, T] \rightarrow \mathbb{R}^c$, where c is the number of channels. Given the initial I_0 frames, $\{\mathbf{u}_i = \mathbf{u}(\cdot, t_i) \mid i = 1, \dots, I_0\}$, the task is to predict future solutions.

Each solution frame is discretized as a three-dimensional tensor $\mathbf{u}_t = \mathbf{u}(\cdot, t) \in \mathbb{R}^{N_x \times N_y \times c}$, where N_x and N_y are

Table 1. (Comparison) Summary of Rollout Rescaled L^2 Error (scale by std) for different methods across various cases. The best results are highlighted in bold.

Rollout Rescaled L^2 Error	Case	Ours (single step)	Ours (multi step)	MPP (McCabe et al., 2023)
Step 1 [1e-2]	PDEArena-Incomp	11.10	11.10	6.17
	PDEBench-Comp-LowVis	15.61	15.61	16.37
	PDEBench-Comp-HighVis	5.97	5.97	20.90
Step 5 [1e-2]	PDEArena-Incomp	23.00	25.79	14.81
	PDEBench-Comp-LowVis	24.56	39.54	45.45
	PDEBench-Comp-HighVis	19.73	28.24	42.93
Step 10 [1e-2]	PDEArena-Incomp	36.18	35.02	27.89
	PDEBench-Comp-LowVis	37.47	51.50	64.11
	PDEBench-Comp-HighVis	57.88	79.52	144.46
Last Step [1e-2]	PDEArena-Incomp	77.81	70.83	93.52
	PDEBench-Comp-LowVis	39.03	48.82	65.32
	PDEBench-Comp-HighVis	71.17	96.23	185.29
All average [1e-2]	PDEArena-Incomp	56.27	51.32	55.95
	PDEBench-Comp-LowVis	27.08	36.29	46.68
	PDEBench-Comp-HighVis	30.06	40.06	72.37

the spatial grid sizes. Due to the homogeneous Markovian property, given the initial data $\{\mathbf{u}_t \mid t \geq 0\}$ from some PDE indexed by i_p , for a fixed Δt , there exists an operator $\mathcal{L} = \mathcal{L}_{\Delta t}^{(i_p)}$ that maps frame \mathbf{u}_t to frame $\mathbf{u}_{t+\Delta t}$ for any $t \geq 0$. Our goal is to train a model that learns these operators $\mathcal{L}_{\Delta t}^{(i_p)}$ from the sequence of function pairs generated from the initial frames. Notably, even within the same dataset and fixed Δt , different trajectories can exhibit different dynamics (e.g., due to different Reynolds numbers Re). These variations are implicitly captured by the function pairs in our framework.

4.2. Vision In-Context Operator Networks

The original ICONs represent functions as scattered sample data points, where each data point is projected as a single token. For higher spatial dimensions, this approach necessitates an excessively large number of sample points and extremely long sequences in the transformer. Due to the inherent quadratic complexity of the transformer, this approach becomes computationally infeasible for high-dimensional problems.

Inspired by the Vision Transformer (ViT) (Dosovitskiy, 2020), we address these limitations by dividing the physical fields into patches, where each patch is flattened and projected as a token. This approach, which we call Vision In-Context Operator Networks (VICON), has its forward process illustrated in Figure 1 and detailed in the following.

First, the input \mathbf{u}_t and output $\mathbf{u}_{t+\Delta t}$ functions are divided into patches $\{\mathbf{C}^k \in \mathbb{R}^{R_x \times R_y \times c}\}_{k=1}^{N_c}$ and $\{\mathbf{Q}^l \in \mathbb{R}^{R_x \times R_y \times c}\}_{l=1}^{N_q}$, where R_x, R_y are the resolution dimensions of the patch and N_c and N_q are the number of patches for the input and output functions, respectively. While N_q

can differ from N_c (for instance, when input functions require additional boundary padding, resulting in $N_c > N_q$), we maintain $N_c = N_q$ throughout our experiments. For notational clarity, we add the subscript $i \in \{1, \dots, I\}$ to denote the pair index, where \mathbf{C}_i^k represents the k -th patch of the input function and \mathbf{Q}_i^l represents the l -th patch of the output function in the i -th pair. These patches are then projected into a unified d -dimensional latent embedding space using a shared learnable linear function $f_\phi : R_x \times R_y \times c \rightarrow \mathbb{R}^d$:

$$\begin{aligned} \hat{\mathbf{c}}_i^k &= f_\phi(\mathbf{C}_i^k), \\ \hat{\mathbf{q}}_i^l &= f_\phi(\mathbf{Q}_i^l), \end{aligned} \quad (4)$$

where $k = 1, \dots, N_c$ and $l = 1, \dots, N_q$ index the patches.

We inject two types of learnable positional encoding before feeding the embeddings into the transformer: (1) patch positional encodings to indicate relative patch positions inside the whole domain, denoted as $\mathbf{E}_p \in \mathbb{R}^{N_p \times d}$, where $N_p = \max\{N_c, N_q\}$; (2) function positional encodings to indicate whether a patch belongs to an input function (using $\mathbf{E}_c \in \mathbb{R}^{I \times d}$) or output function (using $\mathbf{E}_q \in \mathbb{R}^{I \times d}$), as well as their indices in the sequence:

$$\begin{aligned} \mathbf{c}_i^k &= \hat{\mathbf{c}}_i^k + \mathbf{E}_p(k) + \mathbf{E}_c(i), \\ \mathbf{q}_i^l &= \hat{\mathbf{q}}_i^l + \mathbf{E}_p(l) + \mathbf{E}_q(i). \end{aligned} \quad (5)$$

The embeddings \mathbf{c}_i^k and \mathbf{q}_i^l are then concatenated to form the input sequence for the transformer:

$$\mathbf{c}_1^1 \dots \mathbf{c}_1^{N_c}, \mathbf{q}_1^1 \dots \mathbf{q}_1^{N_q}, \dots, \mathbf{c}_I^1 \dots \mathbf{c}_I^{N_c}, \mathbf{q}_I^1 \dots \mathbf{q}_I^{N_q}.$$

To support autoregressive prediction similar to Eq 2, VICON employs an alternating-sized (in the case where

Table 2. Summary of Rollout Rescaled L^2 Error Metrics (single step, scale by std) for Ablation Studies across various cases. The best results are highlighted in bold. Columns: N = PDEArena-Incomp only, E = PDEBench-Comp-LowVis only, C = PDEBench-Comp-HighVis only, N + E = PDEArena-Incomp + PDEBench-Comp-LowVis, N + C = PDEArena-Incomp + PDEBench-Comp-HighVis, E + C = PDEBench-Comp-LowVis + PDEBench-Comp-HighVis. All ablation groups have equal dataset batch sizes, adding up to 30. The best results are marked with **bold**, 2nd-best with underline.

Rollout Rescaled L^2 Error [1e-2]	Case	All included	N	E	C	N + E	N + C	E + C
Step 1	PDEArena-Incomp	11.10	6.72	54.26	58.63	11.11	<u>7.84</u>	53.69
	PDEBench-Comp-LowVis	15.61	88.24	13.59	46.66	14.86	45.96	<u>14.08</u>
	PDEBench-Comp-HighVis	5.79	216.50	49.68	2.81	38.38	<u>3.28</u>	4.65
Step 5	PDEArena-Incomp	23.00	14.18	105.19	85.76	22.95	<u>16.25</u>	100.12
	PDEBench-Comp-LowVis	24.56	106.29	22.10	67.27	23.88	68.15	<u>22.53</u>
	PDEBench-Comp-HighVis	19.73	584.50	170.20	7.49	141.22	<u>8.38</u>	12.41
Step 10	PDEArena-Incomp	36.18	23.90	147.28	110.04	36.87	<u>26.63</u>	142.60
	PDEBench-Comp-LowVis	37.47	119.84	33.94	81.27	36.43	82.27	<u>34.49</u>
	PDEBench-Comp-HighVis	57.88	1903.41	514.88	20.26	410.23	<u>22.65</u>	33.42
Last Step	PDEArena-Incomp	77.81	69.95	289.62	185.34	86.16	<u>71.90</u>	294.19
	PDEBench-Comp-LowVis	39.03	120.74	35.16	83.24	37.61	84.19	<u>35.70</u>
	PDEBench-Comp-HighVis	71.17	2356.29	626.60	24.35	495.02	<u>27.28</u>	40.24
All average	PDEArena-Incomp	56.26	44.35	202.67	142.00	59.65	<u>47.31</u>	203.04
	PDEBench-Comp-LowVis	27.08	107.54	24.35	68.71	26.27	69.52	<u>24.83</u>
	PDEBench-Comp-HighVis	30.06	956.67	263.98	10.91	213.34	<u>12.25</u>	18.06

$N_c \neq N_q$) block causal attention mask, as opposed to the conventional triangular causal attention mask as in mainstream generative large language models (Brown et al., 2020) and large vision models (Bai et al., 2024). The mask is defined as follows:

$$\mathbf{M} = \begin{bmatrix} \mathbf{1}_{N_c, N_c} & \mathbf{0} & \cdots & \mathbf{0} & \mathbf{0} \\ \mathbf{1}_{N_q, N_c} & \mathbf{1}_{N_q, N_q} & \cdots & \mathbf{0} & \mathbf{0} \\ \vdots & \vdots & \ddots & \vdots & \vdots \\ \mathbf{1}_{N_c, N_c} & \mathbf{1}_{N_c, N_q} & \cdots & \mathbf{1}_{N_c, N_c} & \mathbf{0} \\ \mathbf{1}_{N_q, N_c} & \mathbf{1}_{N_q, N_q} & \cdots & \mathbf{1}_{N_q, N_c} & \mathbf{1}_{N_q, N_q} \end{bmatrix} \quad (6)$$

where $\mathbf{1}_{m \times n}$ denotes an all-ones matrix of dimension $m \times n$, and $\mathbf{0}$ represents a zero matrix of the corresponding dimensions.

After obtaining the output tokens from Eq 2, we extract the tokens corresponding to the input patch indices $\mathbf{c}_i^1, \dots, \mathbf{c}_i^{N_c}$ and denote them as $\tilde{\mathbf{q}}_i^1, \dots, \tilde{\mathbf{q}}_i^{N_c}$. These tokens are then projected back to the original physical space using a shared learnable linear function $g_\psi : \mathbb{R}^d \rightarrow \mathbb{R}^{R_x \times R_y \times c}$:

$$\tilde{\mathbf{Q}}_i^l = g_\psi(\tilde{\mathbf{q}}_i^l), \quad (7)$$

which predicts \mathbf{Q}_i^l .

Throughout our experiments, we set $I_{\min} = 5$ in-context example pairs, providing at least five examples to ensure sufficient information about the dynamics before evaluating errors.

4.3. Prompt Normalization

To address the varying scales across different channels and prompts (i.e. sequences of pairs $\{(\mathbf{c}_i, \mathbf{q}_i)\}_{i=1}^I$), we normalize the data before feeding them into the model. A crucial

requirement is to consistently normalize functions within the same sequence, to ensure that the same operator is learned. Denoting the normalization operators for \mathbf{c} and \mathbf{q} as \mathcal{N}_c and \mathcal{N}_q respectively, and the operator in the original space as \mathcal{L} , the operator in the normalized space \mathcal{L}' follows:

$$\mathcal{L}'(\mathcal{N}_c(\mathbf{u})) = \mathcal{N}_q(\mathcal{L}(\mathbf{u})), \quad (8)$$

or equivalently:

$$\mathcal{L}'(\mathbf{v}) = \mathcal{N}_q(\mathcal{L}(\mathcal{N}_c^{-1}(\mathbf{v}))).$$

In this work, we simply set $\mathcal{N}_c = \mathcal{N}_q$, mainly because our maximum timestep stride $s_{\max} = 5$ is relatively small (i.e., the scale distribution does not change dramatically). Specifically, we computed the channel-wise mean μ and standard deviation σ of $\{\mathbf{c}_i\}_{i=1}^I$ in each prompt, then used these values to normalize $\{(\mathbf{c}_i, \mathbf{q}_i)\}_{i=1}^I$ in that prompt. To avoid division by zero, we set a minimum threshold of 10^{-4} for the standard deviation.

4.4. Datasets and Data Augmentation

The dataset used in this work contains three types of equations modeling different fluid dynamics:

1. PDEArena-Incomp (Gupta & Brandstetter, 2022), the incompressible Navier-Stokes (NS) equation
2. PDEBench-Comp-HighVis (Takamoto et al., 2022), the compressible NS equation
3. PDEBench-Comp-LowVis (Takamoto et al., 2022), the compressible NS equation with very low viscosity

Detailed descriptions of the datasets are provided in Appendix A.

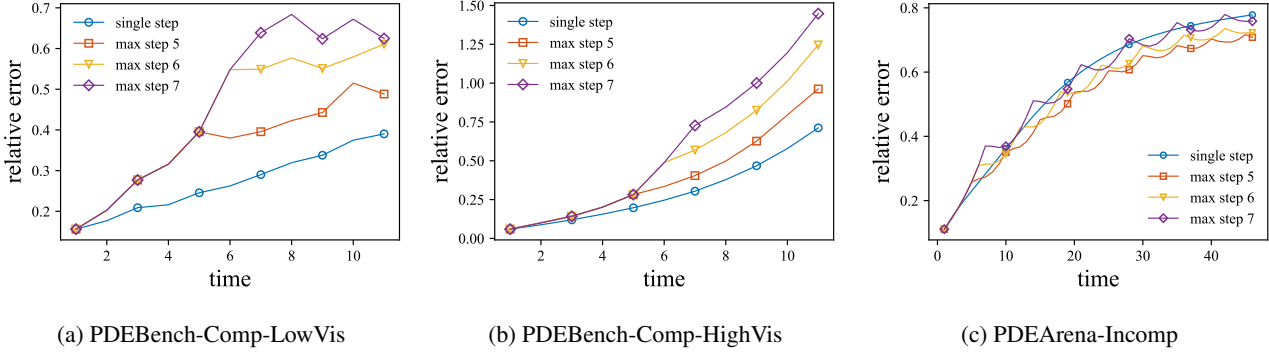


Figure 2. Comparison of rollout errors across different datasets, using single-step and multi-step strategies with varying maximum step sizes ($s_{\max} = 5, 6, 7$).

The temporally homogeneous Markovian property (Section 4.1) enables natural data augmentation for training and flexible rollout strategy for inference (Section 4.5): by striding with larger timesteps to reduce the number of autoregressive steps in long-term prediction tasks: $\Delta t = s\Delta\tau_{i_p} \mid s = 1, 2, \dots, s_{\max}$, where τ_{i_p} is the timestep size for recording in trajectory i_p . During training, for each trajectory in the dataset, we first sample a stride size $s \sim \mathcal{U}\{1, \dots, s_{\max}\}$, then form $\langle \mathbf{u}_t, \mathbf{u}_{t+s\Delta\tau} \rangle$ pairs for the corresponding operator.

4.5. Inference with Flexible Strategies

As mentioned in Section 4.4, VICON can make predictions with varying timestep strides. Given I_0 initial frames $\{\mathbf{u}_i\}_{i=1}^{I_0}$, we can form in-context example pairs $\{\langle \mathbf{u}_i, \mathbf{u}_{i+s} \rangle\}_{i=1}^{I_0-s}$. For $j \geq 1$, we set the question condition (\mathbf{c}_k in Equation 3) as \mathbf{u}_j to predict \mathbf{u}_{j+s} , enabling s -step prediction.

For long-term rollout, we employ VICON in an autoregressive fashion. The ability to predict with different timestep strides enables various rollout strategies. We explore two natural approaches: single-step rollout and multi-step rollout, where the latter advances in larger strides to reduce the number of rollout steps.

For single-step rollout, we simply follow the autoregressive procedure with $s = 1$. Multi-step rollout involves a more sophisticated approach: given a maximum prediction stride s_{\max} , we first make sequential predictions with a gradually growing $s = 1$ to s_{\max} using \mathbf{u}_{I_0} as the question condition, obtaining $\{\mathbf{u}_{I_0+s}\}_{s=1}^{s_{\max}}$. Using each frame in this sequence as a question condition, we then make consistent s_{\max} -step predictions while preserving all intermediate frames. This multi-step strategy follows the approach in (Yang & Osher, 2024). Detailed examples of both rollout strategies are provided in Appendix B.3.

4.6. Evaluation Metric

We evaluate the rollout accuracy of VICON using two different strategies described in Section 4.5. The evaluation uses rescaled and absolute L^2 errors between the predicted and ground truth frames, starting from the frame $I_0 + 1$. For relative scaling coefficients, we use channel-wise scaling standard deviation σ of ground truth frames, which vary between different prompts.

5. Experimental Results

The detailed experimental results are presented in Table 1 and Table 8, where we report the scaled and absolute L^2 roll-out errors for the three datasets. We record the rollout error at time steps 1, 5, 10, and the last step, along with the average error across all time steps. Due to the flexibility of time steps, a single trained model adopts two rollout strategies: single-step and multistep (Section 4.5) during inference, and we report results for both strategies.

We benchmark against MPP (McCabe et al., 2023) (with the AViT-B model architecture, see details in their Table 3), the current state-of-the-art sequence-to-sequence model. The vanilla ICON, which would require processing over 114K tokens per frame ($128 \times 128 \times 7$), exceeds available GPU memory and is thus computationally infeasible for direct comparison on these datasets.

Superior Accuracy for Long-term Predictions. We observe that VICON (both strategies) outperforms MPP at all timesteps for the PDEBench-Comp-LowVis and PDEBench-Comp-HighVis datasets. For longer rollouts, VICON shows a significant reduction in scaled L^2 error of 40% and 61.6% for PDEBench-Comp-LowVis and PDEBench-Comp-HighVis datasets, respectively. For the PDEArena-Incomp dataset, while VICON slightly underperforms MPP initially, it achieves better results for longer rollouts (the last step and the averaged error across the

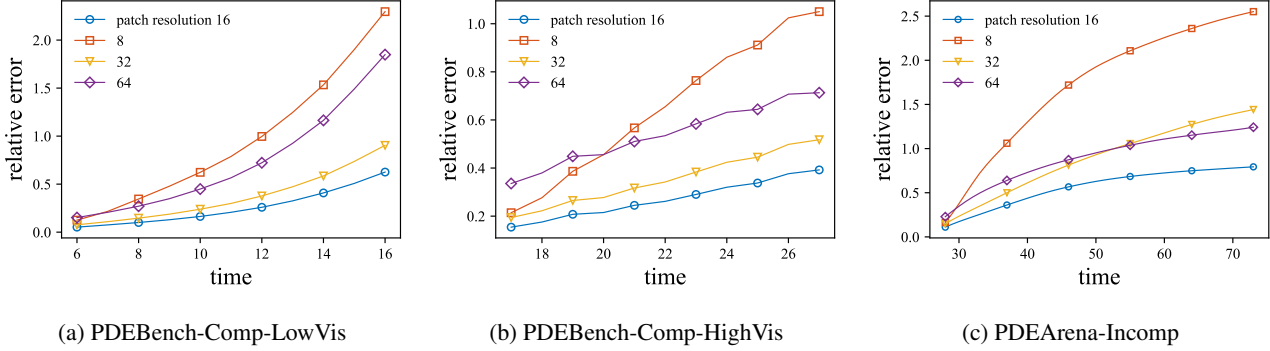


Figure 3. Comparison of rollout errors using different patch resolutions (8, 16, 32, 64).

whole time horizon of 46 steps). In general, our method demonstrates superior long-term predictions compared to MPP.

Turbulence Kinetic Energy Analysis. The turbulence kinetic energy (TKE), defined as $\frac{1}{2}(\tilde{u}_x^2 + \tilde{u}_y^2)$, is a critical metric to quantify the ability of a model to capture turbulent flow characteristics. Here, $\tilde{u} = u - \bar{u}$ denotes the fluctuation of the velocity from its statistical equilibrium state \bar{u} . Within our datasets, only a subset of PDEBench-Comp-LowVis, specifically those initialized with fully developed turbulent fields (see Appendix D.5 of (Takamoto et al., 2022)), is suitable for TKE analysis. After filtering these entries, we compare the mean absolute error (MAE) of the TKE between VICON and MPP. Our approach achieves a TKE error of 0.016, significantly outperforming the MPP’s error of 0.049, which demonstrates superior preservation of turbulent flow characteristics. Figure 4 illustrates a representative comparison of TKE predictions between VICON and MPP.

Flexible Rollout Strategy. To demonstrate the flexibility of our model rollout strategies (Section 4.5), we evaluate the performance of single-step and multi-step rollout strategies with varying maximum step sizes ($s_{\max} = 5, 6, 7$) in Figure 2. We observe that the model performs best with single-step rollout for PDEBench-Comp-LowVis and PDEBench-Comp-HighVis, while multi-step rollout with $s_{\max} = 5$ shows the best performance for PDEArena-Incomp.

This performance difference stems from the datasets’ temporal characteristics: PDEBench-Comp-LowVis and PDEBench-Comp-HighVis use larger timesteps with fewer total frames, making accurate large-stride predictions challenging and favoring single-step approaches. In contrast, PDEArena-Incomp’s longer trajectories with smaller timesteps benefit from multi-step prediction, as reducing the number of rollout steps helps minimize error accumulation.

This flexibility in inference allows the model to adapt to

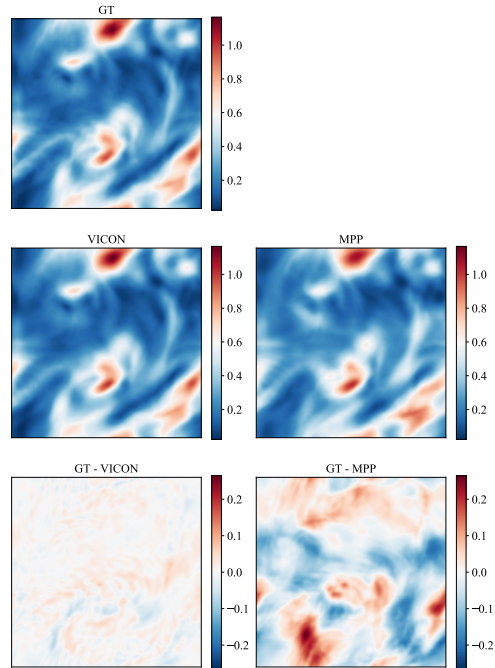


Figure 4. Comparison of turbulence kinetic energy predictions between VICON and MPP, demonstrating the improved accuracy in capturing turbulent flow features of VICON. (Top-left) Ground truth TKE field, (Left) VICON prediction and error, (Right) MPP prediction and error.

different datasets and prediction tasks without retraining, making VICON more versatile for various task settings (such as climate prediction at short and long terms).

Stride Generalization. When evaluated with unseen strides ($s_{\max} = 6, 7$), our model maintains reasonable performance and even outperforms the single-step strategy for PDEArena-Incomp. This capability stems from VICON’s ability to implicitly learn operators via context pairs. When applied to experimental measurements, this ability to extrapolate and generalize to unseen timestep sizes provides

greater tolerance for sampling rates, which can be constrained by hardware limitations.

Computational Efficiency. In Table 3, we compare the computational resources required by VICON and MPP. Our model demonstrates greater efficiency, requiring approximately one third of the inference time per frame and using 75% of the total parameters compared to MPP.

Impact of Patch Resolutions. We conducted ablation studies on patch resolution by varying patch sizes (8, 16, 32, 64). Although smaller patches could theoretically capture finer spatial structures, they generate longer token sequences for the transformer. Due to the quadratic attention complexity, this imposes a critical trade-off: we must reduce the token dimension to stay within memory constraints. Our experiments show that reducing the patch resolution below 16×16 requires lowering both the token dimension from 1024 to 512 and the feedforward dimension from 2048 to 1024 to fit within our GPU memory limits. Moreover, further reduction below the 8×8 patches proved infeasible even with mixed precision training.

The results in Figure 3 demonstrate that our choice of patch size 16 achieves optimal performance in all data sets, indicating an effective balance between the length of the sequence and the representational capacity. Although performance degradation with coarser patches (32, 64) aligns with theoretical expectations, the degradation with finer patch resolution probably stems from the necessary reduction in hidden dimensions. This observation highlights the importance of carefully balancing the sequence length against hidden dimensions. The substantial computational resources required also suggest a fundamental challenge in scaling VICON to 3D applications without stronger computing infrastructure or modifications to the model.

Impact of Data Diversity on Generalization. To evaluate the generalization capabilities of the model across datasets, we performed ablation studies by training on various combinations of datasets. The results are presented in Table 2.

The experiments reveal that the model achieves optimal performance on individual datasets when trained exclusively on them, though at the cost of poor accuracy on others. As more datasets are incorporated during training, a trade-off emerges: Performance on individual datasets slightly decreases, but the model learns to handle different simulation types simultaneously.

These results demonstrate that VICON is a generalized few-shot model for diverse fluid dynamics problems, suggesting potential extensions through additional datasets and pretrain-finetune approaches to address a much wider range of settings.

Table 3. (Comparison) Summary of Resource and Timing Metrics for different methods.

Resource and Timing Metrics	Ours	MPP (McCabe et al., 2023)
Training cost [GPU hrs]	58	64
Rollout time per step [ms]	8.7	25.7
Model Param Size	88M	116M

6. Conclusion and Future Works

We present VICON, a vision-transformer-based in-context operator network that efficiently handles two-dimensional fluid dynamics problems. By processing dense physical fields through patch-wise operations, VICON overcomes the computational limitations of naive ICON approaches while maintaining their flexibility in multi-physics operator learning.

In extensive experiments, we have demonstrated that VICON achieves superior performance compared to existing MPP, especially in long-term predictions. VICON also offers flexible rollout strategies with varying time-step strides, allowing users to adapt predictions based on specific scenario requirements.

Several promising directions remain for future investigation. Our method currently requires full domain input. 1. Incorporating physical priors, such as translational invariance, could enable domain decomposition for training on smaller subdomains, effectively decoupling computational complexity from domain size. 2. Extending VICON to handle irregular domains and different data structures such as graphs or point clouds would broaden its applicability to more realistic scenarios. 3. Our current approach of joining channels across datasets has limited scalability. Drawing inspiration from machine translation’s subword tokenization, developing adaptive physical field representations could offer a more scalable cross-dataset solution. 4. Most critically, extending to 3D applications faces fundamental challenges as token sequence length grows cubically with spatial dimensions, while memory constraints limit the hidden dimensions and representational capacity. Novel architectures combining in-context learning with efficient data compression techniques may be necessary to address this limitation.

Acknowledgment

Yadi Cao and Rose Yu are supported in part by the US Army Research Office under Army-ECASE award W911NF-23-1-0231, the US Department of Energy, Office of Science, IARPA HAYSTAC Program, CDC-RFA-FT-23-0069, DARPA AIE FoundSci, DARPA YFA, NSF grants #2205093, #2100237, #2146343, and #2134274. Yuxuan Liu and Hayden Schaeffer are supported in part by AFOSR MURI FA9550-21-1-0084 and NSF DMS 2427558. Liu

Yang is supported by the NUS Presidential Young Professorship. Stanley Osher is partially funded by STROBE NSF STC887 DMR 1548924, AFOSR MURI FA9550-18-502 and ONR N00014-20-1-2787.

Impact Statement

This paper presents work whose goal is to advance the field of Machine Learning. There are many potential societal consequences of our work, none which we feel must be specifically highlighted here.

References

- Bai, Y., Geng, X., Mangalam, K., Bar, A., Yuille, A. L., Darrell, T., Malik, J., and Efros, A. A. Sequential modeling enables scalable learning for large vision models. In *Proceedings of the IEEE/CVF Conference on Computer Vision and Pattern Recognition*, pp. 22861–22872, 2024.
- Brown, T., Mann, B., Ryder, N., Subbiah, M., Kaplan, J. D., Dhariwal, P., Neelakantan, A., Shyam, P., Sastry, G., Askell, A., and others. Language models are few-shot learners. *Advances in neural information processing systems*, 33:1877–1901, 2020.
- Cao, S. Choose a transformer: Fourier or galerkin. *Advances in neural information processing systems*, 34: 24924–24940, 2021.
- Cao, Y., Chai, M., Li, M., and Jiang, C. Efficient learning of mesh-based physical simulation with bi-stride multi-scale graph neural network. In *International Conference on Machine Learning*, pp. 3541–3558, 2023.
- Chen, T. and Chen, H. Approximation capability to functions of several variables, nonlinear functionals, and operators by radial basis function neural networks. *IEEE Transactions on Neural Networks*, 6(4):904–910, 1995a.
- Chen, T. and Chen, H. Universal approximation to nonlinear operators by neural networks with arbitrary activation functions and its application to dynamical systems. *IEEE transactions on neural networks*, 6(4):911–917, 1995b.
- Chen, W., Song, J., Ren, P., Subramanian, S., Morozov, D., and Mahoney, M. W. Data-efficient operator learning via unsupervised pretraining and in-context learning. *arXiv preprint arXiv:2402.15734*, 2024.
- Dosovitskiy, A. An image is worth 16x16 words: Transformers for image recognition at scale. *arXiv preprint arXiv:2010.11929*, 2020.
- E, W. and Yu, B. The deep Ritz method: a deep learning-based numerical algorithm for solving variational problems. *Commun. Math. Stat.*, 6(1):1–12, 2018. ISSN 2194-6701. doi: 10.1007/s40304-018-0127-z. URL <https://doi.org/10.1007/s40304-018-0127-z>.
- Gupta, J. K. and Brandstetter, J. Towards multi-spatiotemporal-scale generalized pde modeling. *arXiv preprint arXiv:2209.15616*, 2022.
- Herde, M., Raonić, B., Rohner, T., Käppeli, R., Molinaro, R., Bézenac, E., and Mishra, S. Poseidon: Efficient foundation models for pdes. *arXiv preprint arXiv:2405.19101*, 2024.

- Jiang, Z., Zhu, M., and Lu, L. Fourier-mionet: Fourier-enhanced multiple-input neural operators for multiphase modeling of geological carbon sequestration. *Reliability Engineering & System Safety*, 251:110392, 2024.
- Jin, P., Meng, S., and Lu, L. Mionet: Learning multiple-input operators via tensor product. *SIAM Journal on Scientific Computing*, 44(6):A3490–A3514, 2022.
- Jollie, D., Sun, J., Zhang, Z., and Schaeffer, H. Time-series forecasting, knowledge distillation, and refinement within a multimodal pde foundation model. *arXiv preprint arXiv:2409.11609*, 2024.
- Kovachki, N., Li, Z., Liu, B., Azizzadenesheli, K., Bhattacharya, K., Stuart, A., and Anandkumar, A. Neural operator: Learning maps between function spaces with applications to PDEs. *Journal of Machine Learning Research*, 24(89):1–97, 2023.
- Li, S., Zhao, Y., Varma, R., Salpekar, O., Noordhuis, P., Li, T., Paszke, A., Smith, J., Vaughan, B., Damania, P., and others. Pytorch distributed: Experiences on accelerating data parallel training. *arXiv preprint arXiv:2006.15704*, 2020.
- Li, Z., Kovachki, N. B., Azizzadenesheli, K., liu, B., Bhattacharya, K., Stuart, A., and Anandkumar, A. Fourier neural operator for parametric partial differential equations. In *International Conference on Learning Representations*, 2021. URL <https://openreview.net/forum?id=c8P9NQVtmnO>.
- Li, Z., Meidani, K., and Farimani, A. B. Transformer for partial differential equations’ operator learning. *arXiv preprint arXiv:2205.13671*, 2022.
- Li, Z., Kovachki, N., Choy, C., Li, B., Kossaifi, J., Otta, S., Nabian, M. A., Stadler, M., Hundt, C., Azizzadenesheli, K., and others. Geometry-informed neural operator for large-scale 3d pdes. *Advances in Neural Information Processing Systems*, 36, 2024.
- Lino, M., Fotiadis, S., Bharath, A. A., and Cantwell, C. D. Multi-scale rotation-equivariant graph neural networks for unsteady eulerian fluid dynamics. *Physics of Fluids*, 34(8):087110, 2022.
- Liu, Y., Sun, J., He, X., Pinney, G., Zhang, Z., and Schaeffer, H. Prose-fd: A multimodal pde foundation model for learning multiple operators for forecasting fluid dynamics. *arXiv preprint arXiv:2409.09811*, 2024a.
- Liu, Y., Zhang, Z., and Schaeffer, H. Prose: Predicting multiple operators and symbolic expressions using multimodal transformers. *Neural Networks*, 180:106707, 2024b.
- Lorsung, C., Li, Z., and Farimani, A. B. Physics informed token transformer for solving partial differential equations. *Machine Learning: Science and Technology*, 5(1):015032, 2024.
- Lu, L., Jin, P., Pang, G., Zhang, Z., and Karniadakis, G. E. Learning nonlinear operators via DeepONet based on the universal approximation theorem of operators. *Nature machine intelligence*, 3(3):218–229, 2021.
- Lu, L., Meng, X., Cai, S., Mao, Z., Goswami, S., Zhang, Z., and Karniadakis, G. E. A comprehensive and fair comparison of two neural operators (with practical extensions) based on fair data. *Computer Methods in Applied Mechanics and Engineering*, 393:114778, 2022.
- McCabe, M., Régaldo-Saint Blancard, B., Parker, L. H., Ohana, R., Cranmer, M., Bietti, A., Eickenberg, M., Golkar, S., Krawezik, G., Lanusse, F., and others. Multiple physics pretraining for physical surrogate models. In *NeurIPS 2023 AI for Science Workshop*, 2023.
- Moya, C., Mollaali, A., Zhang, Z., Lu, L., and Lin, G. Conformalized-deeponet: A distribution-free framework for uncertainty quantification in deep operator networks. *arXiv preprint arXiv:2402.15406*, 2024.
- Paszke, A., Gross, S., Massa, F., Lerer, A., Bradbury, J., Chanan, G., Killeen, T., Lin, Z., Gimelshein, N., Antiga, L., and others. Pytorch: An imperative style, high-performance deep learning library. *Advances in neural information processing systems*, 32, 2019.
- Pathak, J., Subramanian, S., Harrington, P., Raja, S., Chattopadhyay, A., Mardani, M., Kurth, T., Hall, D., Li, Z., Azizzadenesheli, K., and others. Fourcastnet: A global data-driven high-resolution weather model using adaptive fourier neural operators. *arXiv preprint arXiv:2202.11214*, 2022.
- Raissi, M., Perdikaris, P., and Karniadakis, G. E. Physics-informed neural networks: a deep learning framework for solving forward and inverse problems involving nonlinear partial differential equations. *J. Comput. Phys.*, 378:686–707, 2019. ISSN 0021-9991. doi: 10.1016/j.jcp.2018.10.045. URL <https://doi.org/10.1016/j.jcp.2018.10.045>.
- Ramesh, A., Pavlov, M., Goh, G., Gray, S., Voss, C., Radford, A., Chen, M., and Sutskever, I. Zero-shot text-to-image generation. In *International conference on machine learning*, pp. 8821–8831. Pmlr, 2021.
- Sanchez-Gonzalez, A., Godwin, J., Pfaff, T., Ying, R., Leskovec, J., and Battaglia, P. Learning to simulate complex physics with graph networks. In *International conference on machine learning*, pp. 8459–8468. PMLR, 2020.

- Schaeffer, H. Learning partial differential equations via data discovery and sparse optimization. *Proceedings of the Royal Society A: Mathematical, Physical and Engineering Sciences*, 473(2197):20160446, 2017.
- Sirignano, J. and Spiliopoulos, K. DGM: a deep learning algorithm for solving partial differential equations. *J. Comput. Phys.*, 375:1339–1364, 2018. ISSN 0021-9991. doi: 10.1016/j.jcp.2018.08.029. URL <https://doi.org/10.1016/j.jcp.2018.08.029>.
- Sun, J., Liu, Y., Zhang, Z., and Schaeffer, H. Towards a foundation model for partial differential equation: Multi-operator learning and extrapolation. *arXiv preprint arXiv:2404.12355*, 2024a.
- Sun, J., Zhang, Z., and Schaeffer, H. Lemon: Learning to learn multi-operator networks. *arXiv preprint arXiv:2408.16168*, 2024b.
- Takamoto, M., Praditia, T., Leiteritz, R., MacKinlay, D., Alesiani, F., Pflüger, D., and Niepert, M. Pdebench: An extensive benchmark for scientific machine learning. *Advances in Neural Information Processing Systems*, 35: 1596–1611, 2022.
- Touvron, H., Lavril, T., Izacard, G., Martinet, X., Lachaux, M., Lacroix, T., Rozière, B., Goyal, N., Hambro, E., Azhar, F., and others. LLaMA: Open and efficient foundation language models. *arXiv preprint arXiv:2302.13971*, 2023.
- Wang, H., Cao, Y., Huang, Z., Liu, Y., Hu, P., Luo, X., Song, Z., Zhao, W., Liu, J., Sun, J., and others. Recent advances on machine learning for computational fluid dynamics: A survey. *arXiv preprint arXiv:2408.12171*, 2024.
- Wang, S., Wang, H., and Perdikaris, P. Learning the solution operator of parametric partial differential equations with physics-informed DeepONets. *Science Advances*, 7(40): eabi8605, 2021.
- Wen, G., Li, Z., Azizzadenesheli, K., Anandkumar, A., and Benson, S. M. U-fno—an enhanced fourier neural operator-based deep-learning model for multiphase flow. *Advances in Water Resources*, 163:104180, 2022.
- Yang, L. and Osher, S. J. PDE generalization of in-context operator networks: A study on 1D scalar nonlinear conservation laws. *Journal of Computational Physics*, 519:113379, 2024. ISSN 0021-9991. doi: <https://doi.org/10.1016/j.jcp.2024.113379>. URL <https://www.sciencedirect.com/science/article/pii/S0021999124006272>.
- Yang, L., Liu, S., Meng, T., and Osher, S. J. In-context operator learning with data prompts for differential equation problems. *Proceedings of the National Academy of Sciences*, 120(39):e2310142120, 2023a.
- Yang, L., Liu, S., and Osher, S. J. Fine-tune language models as multi-modal differential equation solvers. *arXiv preprint arXiv:2308.05061*, 2023b.
- Ye, Z., Huang, X., Chen, L., Liu, Z., Wu, B., Liu, H., Wang, Z., and Dong, B. Pdeformer-1: A foundation model for one-dimensional partial differential equations. *arXiv preprint arXiv:2407.06664*, 2024.
- Yin, M., Charon, N., Brody, R., Lu, L., Trayanova, N., and Maggioni, M. Dimon: Learning solution operators of partial differential equations on a diffeomorphic family of domains. *arXiv preprint arXiv:2402.07250*, 2024.
- Zhang, Z., Wing Tat, L., and Schaeffer, H. Belnet: basis enhanced learning, a mesh-free neural operator. *Proceedings of the Royal Society A*, 479(2276):20230043, 2023.
- Zhang, Z., Moya, C., Leung, W. T., Lin, G., and Schaeffer, H. Bayesian deep operator learning for homogenized to fine-scale maps for multiscale pde. *Multiscale Modeling & Simulation*, 22(3):956–972, 2024a.
- Zhang, Z., Moya, C., Lu, L., Lin, G., and Schaeffer, H. D2no: Efficient handling of heterogeneous input function spaces with distributed deep neural operators. *Computer Methods in Applied Mechanics and Engineering*, 428: 117084, 2024b.
- Zhang, Z., Moya, C., Lu, L., Lin, G., and Schaeffer, H. Deeponet as a multi-operator extrapolation model: Distributed pretraining with physics-informed fine-tuning. *arXiv preprint arXiv:2411.07239*, 2024c.

A. Dataset Details

A.1. PDEArena-Incomp Dataset

The incompressible Navier-Stokes dataset comes from PDEArena (Gupta & Brandstetter, 2022). The data are generated from the equation

$$\partial_t \mathbf{u} + \mathbf{u} \cdot \nabla \mathbf{u} = -\nabla p + \mu \Delta \mathbf{u} + \mathbf{f}, \quad (9)$$

$$\nabla \cdot \mathbf{u} = 0. \quad (10)$$

The space-time domain is $[0, 32]^2 \times [18, 105]$ where $dt = 1.5$ and the space resolution is 128×128 . A scalar particle field is being transported with the fluids. The velocity fields satisfy Dirichlet boundary condition, and the scalar field satisfies Neumann boundary condition. The forcing term \mathbf{f} is randomly sampled. The quantities of interest are the velocities and the scalar particle field.

A.2. PDEBench-Comp-HighVis and PDEBench-Comp-LowVis Datasets

The PDEBench-Comp-HighVis and PDEBench-Comp-LowVis datasets come from PDEBench Compressible Navier-Stokes dataset (Takamoto et al., 2022). The data are generated from the equation

$$\partial_t \rho + \nabla \cdot (\rho \mathbf{u}) = 0, \quad (11)$$

$$\rho(\partial_t \mathbf{u} + \mathbf{u} \cdot \nabla \mathbf{u}) = -\nabla p + \eta \Delta \mathbf{u} + (\zeta + \eta/3) \nabla(\nabla \cdot \mathbf{u}), \quad (12)$$

$$\partial_t \left(\varepsilon + \frac{\rho u^2}{2} \right) = -\nabla \cdot \left(\left(\varepsilon + p + \frac{\rho u^2}{2} \right) \mathbf{u} - \mathbf{u} \cdot \sigma' \right). \quad (13)$$

The space-time domain is $\mathbb{T}^2 \times [0, 1]$ where $dt = 0.05$. The datasets contain different combinations of shear and bulk viscosities. We group the ones with larger viscosities into the PDEBench-Comp-HighVis dataset, and the ones with extremely small (1e-8) viscosities into the PDEBench-Comp-LowVis dataset. The PDEBench-Comp-HighVis dataset has space resolution 128×128 . The PDEBench-Comp-LowVis dataset has raw space resolution 512×512 and is downsampled to 128×128 through average pooling for consistency. The quantities of interest are velocities, pressure, and density.

A.3. QOI Union and Channel Mask

Since each dataset contains different sets of quantities of interest, we take their union to create a unified representation. The unified physical field has 7 channels in total, with the following ordering:

1. Density (ρ)
2. Velocity at x direction (u_x)
3. Velocity at y direction (u_y)
4. Pressure (P)
5. Vorticity (ω)
6. Passively transported scalar field (S)
7. Node type indicator (0: interior node, 1: boundary node)

For each dataset, we use a channel mask to indicate its valid fields and only calculate loss on these channels. The node type channel is universally excluded from loss calculations across all datasets.

B. Experiment Details

B.1. VICON Model Details

Here we provide key architectural parameters of VICON model implementation in Table 4.

Table 4. Model Configuration Details

Key Hyperparameters & Shapes	
<i>Patch Configuration</i>	
Input patch numbers	8 × 8
Output patch numbers	8 × 8
Patch resolution	16 × 16
<i>Positional Encodings Shapes</i>	
Patch positional encodings	[64, 1024]
Function positional encodings	[20, 1024]
<i>Transformer Configuration</i>	
Hidden dimension	1024
Number of attention heads	8
Feedforward dimension	2048
Number of layers	10
Dropout rate	0.0
Number of COND & QOI pairs	10

B.2. Training Details

We implement our method in PyTorch (Paszke et al., 2019) and utilize data parallel training (Li et al., 2020) across two NVIDIA RTX 4090 GPUs. We employ the AdamW optimizer with a cosine learning rate schedule that includes a linear warmup phase. We apply gradient clipping with a maximum norm of 1.0 to ensure training stability. All optimization parameters are detailed in Table 5.

Table 5. Optimization Hyperparameters

Parameter	Value
<i>Learning Rate Schedule</i>	
Scheduler	Cosine Annealing with Linear Warmup
Peak learning rate	1×10^{-4}
Final learning rate	1×10^{-7}
Warmup steps	20,000
Total steps	200,000
<i>Optimization Settings</i>	
Optimizer	AdamW
Weight decay	1×10^{-4}
Gradient norm clip	1.0

B.3. Rollout Strategy Example

We demonstrate two rollout strategies in Tables 6 and 7, showing single-step and multi-step strategies, respectively. In both cases, the initial frames span from time step 0 to 9, and we aim to predict the trajectory up to time step 20.

Table 6. Single-step Rollout Strategy Example

Rollout index	Example CONDs	Example QOIs	Question COND	Predict QOI
1	[0,1,2,3,4,5,6,7,8]	[1,2,3,4,5,6,7,8,9]	9	10
2	[0,1,2,3,4,5,6,7,8]	[1,2,3,4,5,6,7,8,9]	10	11
3	[0,1,2,3,4,5,6,7,8]	[1,2,3,4,5,6,7,8,9]	11	12
4	[0,1,2,3,4,5,6,7,8]	[1,2,3,4,5,6,7,8,9]	12	13
5	[0,1,2,3,4,5,6,7,8]	[1,2,3,4,5,6,7,8,9]	13	14
6	[0,1,2,3,4,5,6,7,8]	[1,2,3,4,5,6,7,8,9]	14	15
7	[0,1,2,3,4,5,6,7,8]	[1,2,3,4,5,6,7,8,9]	15	16
8	[0,1,2,3,4,5,6,7,8]	[1,2,3,4,5,6,7,8,9]	16	17
9	[0,1,2,3,4,5,6,7,8]	[1,2,3,4,5,6,7,8,9]	17	18
10	[0,1,2,3,4,5,6,7,8]	[1,2,3,4,5,6,7,8,9]	18	19
11	[0,1,2,3,4,5,6,7,8]	[1,2,3,4,5,6,7,8,9]	19	20

As shown in Table 7, the multi-step strategy initially uses smaller strides to build sufficient examples, then employs maximum strides for later rollouts, as detailed in Section 4.5. We note that repeated in-context examples appear in Table 7, which is common when the maximum stride is large and the initial frames cannot form enough examples. While the number of in-context examples in VICON is flexible and our model can accommodate fewer examples than the designed length, our

preliminary experiments indicate that the model performs better with more in-context examples, even when some examples are repeated.

Table 7. Multi-step Rollout Strategy Example ($s_{\max} = 5$)

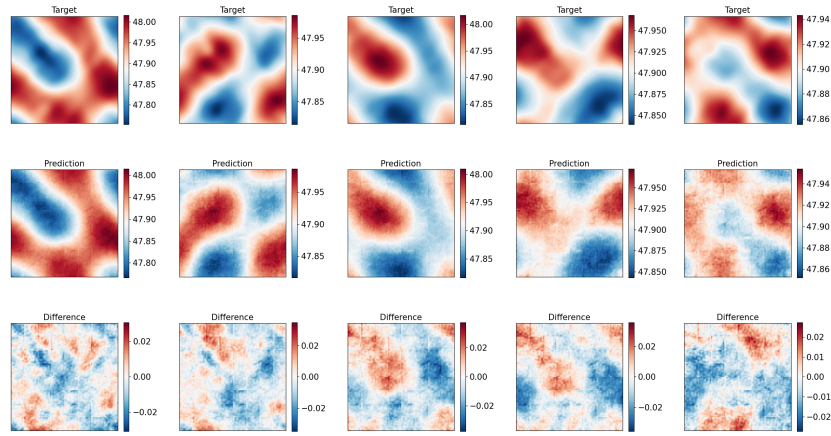
Rollout index	Example CONDs	Example QOIs	Question COND	Predict QOI
1	[0,1,2,3,4,5,6,7,8]	[1,2,3,4,5,6,7,8,9]	9	10
2	[0,0,1,2,3,4,5,6,7]	[2,2,3,4,5,6,7,8,9]	9	11
3	[0,0,1,1,2,3,4,5,6]	[3,3,4,4,5,6,7,8,9]	9	12
4	[0,0,1,1,2,2,3,4,5]	[4,4,5,5,6,6,7,8,9]	9	13
5	[0,0,1,1,2,2,3,3,4]	[5,5,6,6,7,7,8,8,9]	9	14
6	[0,0,1,1,2,2,3,3,4]	[5,5,6,6,7,7,8,8,9]	10	15
7	[0,0,1,1,2,2,3,3,4]	[5,5,6,6,7,7,8,8,9]	11	16
8	[0,0,1,1,2,2,3,3,4]	[5,5,6,6,7,7,8,8,9]	12	17
9	[0,0,1,1,2,2,3,3,4]	[5,5,6,6,7,7,8,8,9]	13	18
10	[0,0,1,1,2,2,3,3,4]	[5,5,6,6,7,7,8,8,9]	14	19
11	[0,0,1,1,2,2,3,3,4]	[5,5,6,6,7,7,8,8,9]	15	20

B.4. MPP (McCabe et al., 2023) Details

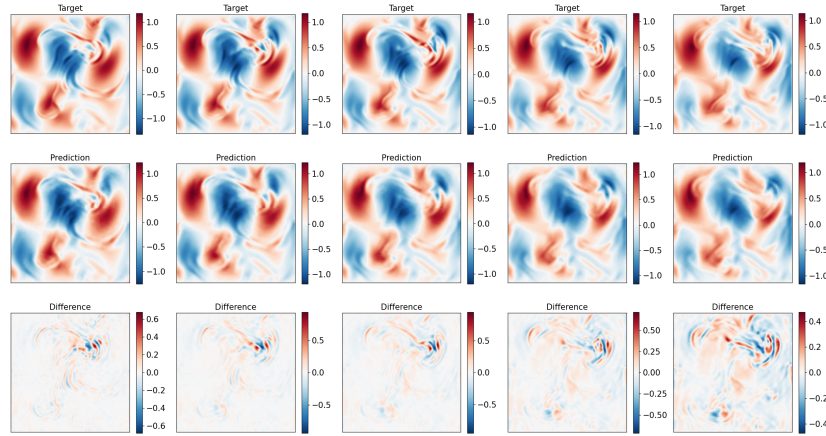
For a fair comparison, we retrained MPP using our training dataset using the same model configurations and optimizer hyperparameters. We evaluate MPP using the same testing setup and metric.

C. More Results and Visualizations

Table 8 summarizes the rollout L^2 errors; Figure 5 and Figure 6 present additional visualizations of the VICON model outputs.

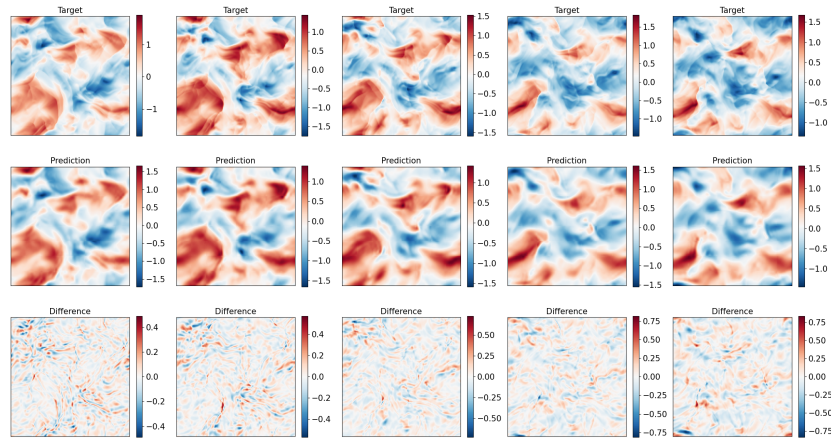


(a) A sequence of 5 output steps for PDEBench-Comp-HighVis dataset. The channel plotted is the pressure field in equation equation 12.

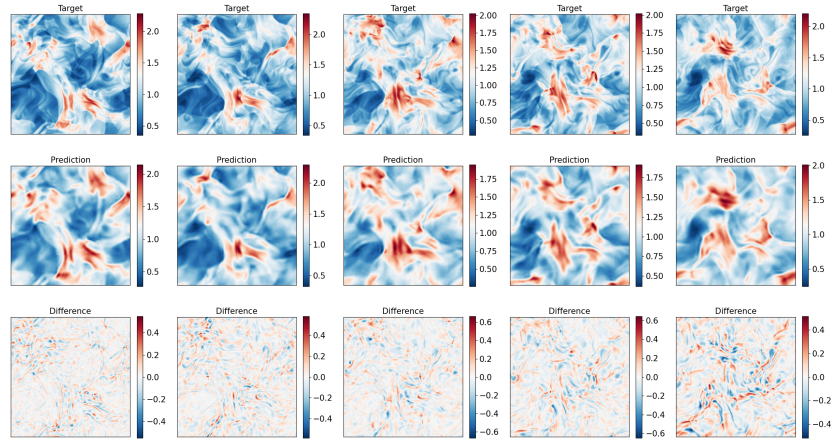


(b) A sequence of 5 output steps for PDEArena-Incomp dataset. The channel plotted is the x-velocity in equation equation 9.

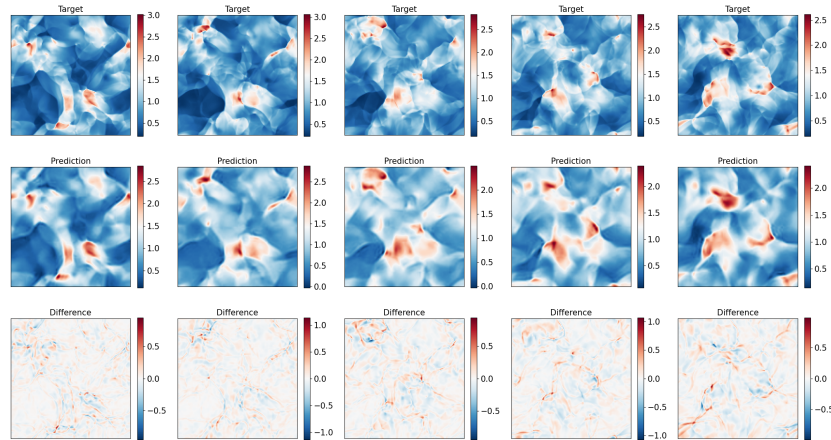
Figure 5. Example outputs for the VICON model. (a) The pressure field of PDEBench-Comp-HighVis dataset, and (b) the x-velocity field of PDEArena-Incomp dataset. Each column represents a different timestep.



(a) The channel plotted is the y-velocity field in equation 9.



(b) The channel plotted is the density field in equation 9.



(c) The channel plotted is the pressure field in equation 9.

Figure 6. More example outputs for the VICON model. Showing 5 output steps for the PDEBench-Comp-LowVis dataset as governed by equation 9: (a) y-velocity, (b) density, and (c) pressure fields. Each column represents a different timestep.

Table 8. (Comparison) Summary of Rollout Absolute L^2 Error for different methods across various cases. The best results are highlighted in bold.

Rollout L^2 Error	Case	Ours (single step)	Ours (multi step)	MPP (McCabe et al., 2023)
Step 1 [1e-2]	PDEArena-Incomp	5.67	5.67	3.12
	PDEBench-Comp-LowVis	21.97	21.97	24.47
	PDEBench-Comp-HighVis	1.55	1.55	4.73
Step 5 [1e-2]	PDEArena-Incomp	10.51	11.83	6.79
	PDEBench-Comp-LowVis	31.46	56.80	57.50
	PDEBench-Comp-HighVis	2.50	6.21	6.52
Step 10 [1e-2]	PDEArena-Incomp	14.82	14.36	11.49
	PDEBench-Comp-LowVis	45.91	65.60	78.54
	PDEBench-Comp-HighVis	3.39	6.49	8.98
Last Step [1e-2]	PDEArena-Incomp	16.82	15.12	19.47
	PDEBench-Comp-LowVis	48.98	63.94	85.60
	PDEBench-Comp-HighVis	3.58	6.24	9.56
All average [1e-2]	PDEArena-Incomp	16.64	15.18	15.77
	PDEBench-Comp-LowVis	34.73	50.21	60.68
	PDEBench-Comp-HighVis	2.64	4.85	7.04